# Near-surface seismic characterization from a sparsely sampled field data set

Andrew Mills and Kris Innanen


## ABSTRACT

Multichannel analysis of surface waves (MASW) is a near-surface characterization technique used to estimate shear wave velocities and layer geometries of the shallow subsurface. Typically, MASW uses closely spaced geophones to adequately sample surface waves. In this study, a field data set acquired with greater than ideal receiver separation is used for near-surface velocity inversion.

The least-squares velocity inversion algorithm is developed, for application to shot records containing dispersive ground roll arrivals. The Priddis Thumper Experiment data set, consisting of a 200 m receiver line with 5 m geophone spacing, is used for this study. Individual shot records are stacked, interpolated, and filtered, to reduce spatial aliasing and isolate surface waves. The inversion is then applied to the dispersion curves generated from these processed shot records, producing 1D shear wave velocity profiles. 1D velocity profiles are generated for various source points and combined to produce a 2D velocity profile over the survey line. Bedrock depth is estimated at approximately 20 m, consistent with shallow borehole drill cuttings.


## INTRODUCTION

In fall 2016, CREWES conducted a thumper seismic experiment at the University of Calgary's field research location, on the property of the Rothney Astrophysical Observatory 25 km SW of downtown Calgary. This data set consists of a 200 m survey line, with geophones every 5 m, and a source point at each receiver location. Due to the acquisition parameters, which are on a slightly larger scale than a typical MASW survey, this is a good first test on field data of the processing methods developed in Mills and Innanen (2016). In that study, a processing workflow was developed to increase the resolution of dispersion curves, which are necessary for MASW velocity inversion. This consists of LNMO correcting the shot records to flatten events, interpolating to the desired trace spacing, reversing the LNMO correction, and FK filtering to remove reflections and refractions.

Near-surface shear wave velocities can be estimated by inverting generated dispersion curves. The inversion algorithm developed is a least-squares inversion, following Lines and Treitel (1984). An initial near-surface model is generated from extracted dispersion curves. A synthetic dispersion curve is calculated from this model, and compared to the observed dispersion curve. The difference, or residual between these is measured, and the initial model is perturbed to better match the observed curve. This is iterated until the residual is minimized. The near-surface model generated from this process is the estimated model of the real Earth. This process is applied to the Priddis thumper data set to estimate near-surface shear wave velocities and geometries.

## INVERSION OF DISPERSION CURVES

The inverse problem, in which I wish to re-create the earth model from a measured response, is the opposite of the forward problem, described in Mills et al. (2016). Using the inverse method in this study will allow the prediction of a plausible earth velocity model which could have produced the dispersion response which was measured in the field, or modelled using software.

Once dispersion spectra have been generated from a synthetic or field data set, the fundamental mode curve can be picked, and used to invert for near surface shear wave velocities. Since shear wave velocity controls changes in Rayleigh wave phase velocity (Xia et al., 1999), the shear velocities can be inverted for from Rayleigh wave dispersion curves. I will be utilizing a linear least-squares inversion workflow for the prediction of near surface shear wave velocities (following Lines and Treitel, 1984). The goal of this is to find the model that minimizes the sum of squares of the difference between a synthetically modelled response, and the observed response.

For this study, I am minimizing the error between the synthetic modelled dispersion curve (equation 1a), and an observed dispersion curve (equation 1b), generated from field data or synthetic data. Let the f (number of frequencies) observations of phase velocity be represented by the vector

$$\boldsymbol{d}_{obs} = \begin{bmatrix} y_1 \\ y_2 \\ \vdots \\ y_f \end{bmatrix} \tag{1a}$$

and let the synthetic model phase velocity response be the vector

$$\boldsymbol{d}_{syn} = \begin{bmatrix} s_1 \\ s_2 \\ \vdots \\ s_f \end{bmatrix} \tag{1b}$$

where n is the number of layers.

The inversion procedure involves four steps:

1. The fundamental mode dispersion curve is picked from the observed field or synthetic dispersion spectra.

2. An initial geologic model is estimated from the observed dispersion curve, and a synthetic theoretical dispersion curve is calculated from this model.

3. A least-squares inversion is used to calculate a parameter change vector δ, which will update the initial velocity model.

4. Step 3 is iterated until the error between the observed dispersion curve and predicted dispersion curve is minimized.

The model, and thus the dispersion curve, is a function of several parameters, including Vp, Vs, ρ, number of layers, and layer thickness, which are represented in the model vector θ.

$$\boldsymbol{\theta} = \begin{bmatrix} \boldsymbol{\theta}_1 \\ \boldsymbol{\theta}_2 \\ \vdots \\ \boldsymbol{\theta}_n \end{bmatrix} \tag{2}$$

where n is the number of layers.

**Inversion initialization**

To initialize the inversion, an initial model must be built, whose properties are compared to those in estimated (inverted) models. Dispersion spectra have limited sensitivity to rock density (Xia et al., 1999), so are assumed known. In the case of synthetic tests, the true densities of the model are assigned to the model. In the case of field data tests where density is unknown, densities are assigned to each layer, increasing uniformly with depth. The number of layers for the initial model are chosen based on the shape and spread of the dispersion curve (Figure 1). Dispersion frequencies are chosen where there is a change in phase velocity visible. The high and low frequencies are picked approximately where the curve asymptotically approaches the maximum and minimum velocities. The rest of the points are picked where changes are visible, and where the different frequencies are likely to predict sufficiently thick layers. For example, picking 10, 11, 12 Hz will likely predict three very thin layers, which are unlikely to have been sufficiently resolved in the data. Here, picking 10 and 13 Hz is sufficient.

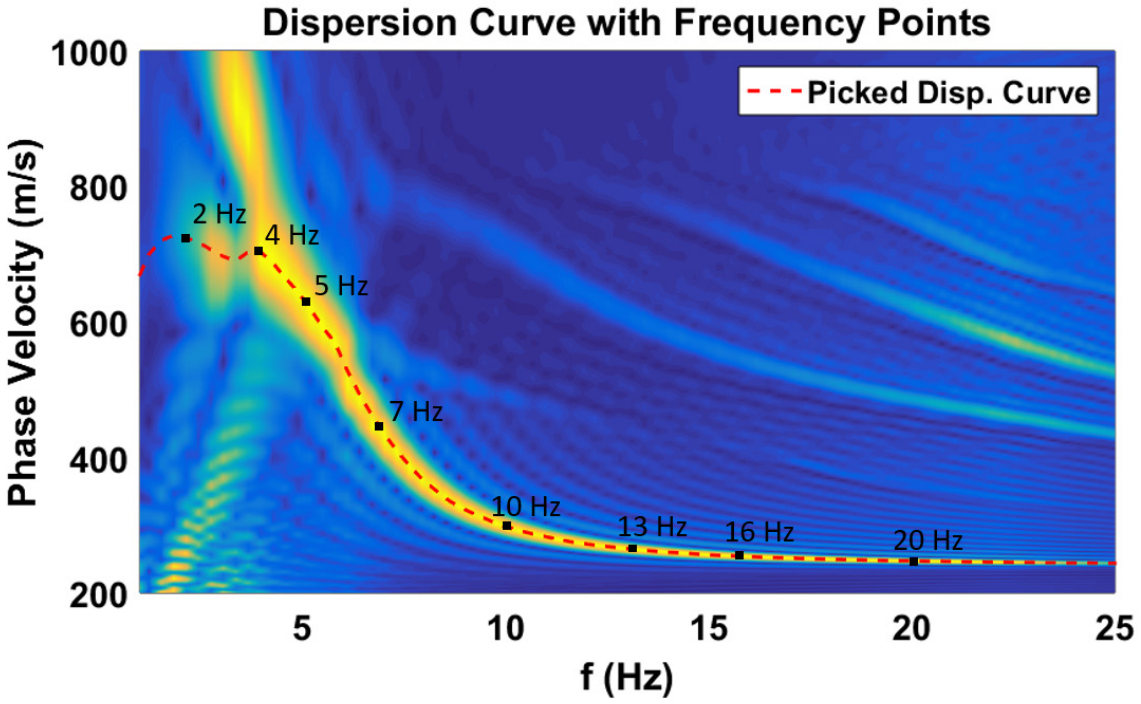


FIG. 1. Dispersion curve with picked frequency points to be used in initial model estimation.

Layer velocities, thicknesses, and depths are calculated using relationships derived in Xia et al. (1999), as follows:

$$Vs_1 = \frac{V_r(high)}{0.88} \text{ (for the first layer)}$$

$$Vs_n = \frac{V_r(low)}{0.88} \text{ (for the half-space, n}^{\text{th}} \text{ layer)} \quad (3)$$

$$Vs_i = \frac{V_r(f_i)}{0.88} (i = 2, 3, \ldots, n\text{-}1)$$

where 0.88 is a constant based on Poisson's ratio (Stokoe et al., 1994), as well as modelling trials in Xia et al. (1999). $V_r$(high) is the dispersion phase velocity where the curve approaches the high frequency asymptote, $V_r$(low) is the velocity where the curve approaches the low frequency asymptote, and $V_r(f_i)$ are the velocities from selected frequencies in between. A Vp/Vs ratio of 2 is assumed, allowing simple calculation of P-wave velocities from initial estimated S-wave velocities.

Depths are calculated based on the fact that each wavelength of Rayleigh wave has a different maximum penetration depth, and thus samples a different point in depth. The same frequencies used in velocity calculations, and the calculated shear velocities, are used in equation 4 to calculate depth being sampled.

$$z_n = 0.63\,\lambda = 0.63\,\frac{Vs_n}{f_n} \quad (4)$$

Note that the inversion initialization isn't predicting the layer boundary depths, rather it is predicting the velocity at a point in depth. The layer boundary would lie at an unknown point between adjacent points with different velocities. Once the velocities, depths and thicknesses have been calculated, an initial theoretical dispersion curve can be calculated, as in Mills et al. (2016).

**Least squares inversion**

Recalling that s represents the synthetic model phase velocity, a perturbation of this model can be represented by:

$$\boldsymbol{d_{syn}} = \boldsymbol{d_{syn}^0} + \mathbf{J}\boldsymbol{\delta} \quad (5)$$

where $d_{syn}$ is the updated model's phase velocity vector, $\mathbf{d}_{syn}{}^0$ is the initial model's phase velocity vector, **J** is the f x n Jacobian matrix of partial derivatives (equation 6, 7), and $\boldsymbol{\delta} = \boldsymbol{\theta} - \boldsymbol{\theta}^0$ is the parameter change vector with elements δf representing the changes or perturbations to the S-wave velocity in the model.

$$\mathbf{J}_{fn} = \frac{\partial d_{syn_f}}{\partial \theta_n} = \frac{d_{syn_f}(\theta_n + \delta\theta) - d_{syn_f}(\theta_n)}{\delta\theta} \quad (3.6)$$

$$\mathbf{J}_{\text{fn}} = \begin{bmatrix} \frac{\partial d_{syn_1}}{\partial \theta_1} & \cdots & \frac{\partial d_{syn_1}}{\partial \theta_n} \\ \vdots & \ddots & \vdots \\ \frac{\partial d_{syn_f}}{\partial \theta_1} & \cdots & \frac{\partial d_{syn_f}}{\partial \theta_n} \end{bmatrix} \tag{3.7}$$

Since Vs is the only parameter being inverted for, that is the only model parameter which will be perturbed in **δ**. In equation 3.6, the δθ term is some small change in Vs. The error, or residual between the synthetic response **s** and the observed data **y** is represented by vector **e**:

$$\mathbf{e} = \mathbf{d_{obs}} - \mathbf{d_{syn}} \tag{8}$$

Combining equations 5 and 7 gives:

$$\mathbf{d_{obs}} - (\mathbf{d_{syn}}^{\mathbf{0}} + \mathbf{J\delta}) = \mathbf{e} \tag{9a}$$

$$\mathbf{d_{obs}} - \mathbf{d_{syn}}^{\mathbf{0}} = \mathbf{J\delta} + \mathbf{e} \tag{9b}$$

the left-hand side of 9b gives:

$$\mathbf{g} = \mathbf{d_{obs}} - \mathbf{d_{syn}}^{\mathbf{0}} \tag{10}$$

where the vector **g** is the discrepancy, or residual, vector, the difference between the initial synthetic model's dispersion and the observed dispersion. The cumulative squared error will be defined as:

$$S = \mathbf{e}^{\mathbf{T}}\mathbf{e} \tag{11}$$

In the Gauss-Newton inversion, the normal equations are derived (Lines and Treitel, 1984):

$$\mathbf{J}^{\mathbf{T}}\mathbf{J\delta} = \mathbf{J}^{\mathbf{T}}\mathbf{g} \tag{12}$$

from which a solution for **δ**, the parameter change vector which minimizes a local approximation of the objective function, can be calculated. However, instabilities in Gauss-Newton inversion arise when $\mathbf{J}^{\mathbf{T}}\mathbf{J}$ is nearly singular. When this occurs, the elements of **δ** grow without bound, causing the solution to diverge sharply.

## Regularization

A common, essentially unavoidable issue in geophysical inverse problems is non-uniqueness, i.e., the fact that many models produce the same data (Virieux and Operto, 2009). Regularization is an inversion preconditioning technique used to make the inversion better-posed. Generally, a regularization scheme is one in which additional criteria are used to select one of the infinite number of models honouring the data.

In this research, I regularize the problem using the Marquardt-Levenberg method, also known as damped least-squares. In this method, a constraining condition is imposed on the parameter change vector **δ**. This constraint prevents the unbounded oscillations in the

solution observed with the Gauss-Newton method. A modified form of the normal equations arises from the Marquardt-Levenberg method, yielding

$$\boldsymbol{\delta} = (\mathbf{J}^T\mathbf{J} + \beta\mathbf{I})^{-1}\,\mathbf{J}^T\mathbf{g} \tag{13}$$

where β is a Lagrange multiplier, which can be considered a "damping factor" (Levenberg, 1944), and **I** is the identity matrix. Through limiting the energy of the parameter change vector **δ**, large changes in the model vector **θ** are penalized and the tendency will be to converge on a model. This is a hybrid method, as it strikes a balance between the method of steepest descent and the method of Gauss-Newton least-squares, as shown in Figure 4. A β value of 0 in equation 13 is equivalent to Gauss-Newton least-squares. It is recommended by Lines and Treitel (1984) to set β initially as a large positive value, taking advantage of the good initial convergence properties of the steepest descent method. Absolute numerical values of β, which depend on the units used in the data and model parameters, number of data, number of model parameters, etc., are difficult to gain insight from, nevertheless it was found in this study that setting the β value at 5 produced stable results over enough iterations for the solutions to converge. At each iteration, β is multiplied by 0.8, until it reaches a minimum of 0.5, so that the inversion is weighted towards linear least-squares convergence closer to a solution. With β below 0.5, the instability witnessed originally with the Gauss-Newton method is empirically found to re-emerge.

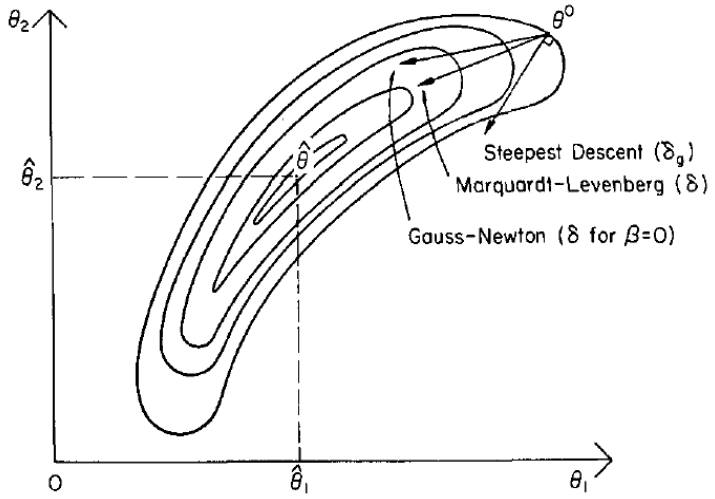


FIG. 4. Geometric relation between the Gauss-Newton, Marquardt-Levenberg, and Steepest Descent solutions, converging towards θ̂ (From Lines and Treitel, 1984).

Gauss-Newton and Marquardt-Levenberg least squares inversion are empirically found to yet be insufficient on their own to accurately predict a plausible earth model; the inversion was found to converge towards models with implausibly high variability between adjacent layers. An additional regularization is added to equation 13 to help constrain and guide the inversion to a more realistic result than would otherwise be found. This regularization, **R**, minimizes the velocity change from one layer to the surrounding layers, reducing extreme velocity variations, and this was found to limit spurious inversion results.

**R** is defined here to minimize the velocity change between subsequent layers,

$$\mathbf{R} = \frac{1}{2}\sum_{i=1}^{n-1}(Vs_n - Vs_{n-1})^2 \tag{14}$$

Taking the first and second derivatives, the R terms to be inserted into the objective function are found:

$$\frac{\partial \mathbf{R}}{\partial \mathbf{Vs_n}} = 2Vs_n - Vs_{n+1} - Vs_{n-1} \tag{15}$$

$$\frac{\partial^2 \mathbf{R}}{\partial \mathbf{Vs_{n1}} \partial \mathbf{Vs_{n2}}} = 2\,\delta(n_1,n_2) - \delta(n_1+1,n_2) - \delta(n_1-1,n_2) \tag{16}$$

By taking the derivative of the objective function with the regularization, Φ, it can be seen where the R terms should be added.

$$\Phi = \frac{1}{2}\left\|d_{obs} - d_{syn}\right\|^2 + R \tag{17}$$

$$\frac{\partial \Phi}{\mathbf{Vs_n}} = \left(d_{obs} - d_{syn}\right)\frac{\partial d_{obs}}{\partial Vs_n} + \frac{\partial R}{\partial Vs_n} \tag{18}$$

This will replace the second term of equation 13:

$$\frac{\partial \Phi}{Vs_n} = \mathbf{J}^T\mathbf{g} + \frac{\partial R}{\partial Vs_n} \tag{19}$$

Taking the second derivative of Φ (equation 20), it is seen that the solution (equation 21) will replace the first term of equation 13:

$$\frac{\partial^2 \Phi}{\partial \mathbf{Vs_{n1}} \partial \mathbf{Vs_{n2}}} = \frac{\partial d_{obs}}{\partial Vs_{n1}}\frac{\partial d_{obs}}{\partial Vs_{n2}} + \frac{\partial^2 R}{\partial Vs_{n1}\,\partial Vs_{n2}} \tag{20}$$

$$\frac{\partial^2 \Phi}{\partial \mathbf{Vs_{n1}} \partial \mathbf{Vs_{n2}}} = \mathbf{J}^T\mathbf{J} + \frac{\partial^2 R}{\partial Vs_{n1}\,\partial Vs_{n2}} \tag{21}$$

The velocity update vector **δ** (equation 13) with the regularization (equations 15, 16) added is:

$$\boldsymbol{\delta}_R = \left((\mathbf{J}^T\mathbf{J} + \lambda\left(\frac{\partial^2 R}{\partial Vs_{n1}\partial Vs_{n2}}\right) + \beta\mathbf{I}\right)^{-1}\left(\mathbf{J}^T\mathbf{g} - \lambda\,\frac{\partial R}{\partial Vs_n}\right) \tag{22}$$

The value λ is the weight applied to the regularization. A higher value will reduce the velocity differences from layer to layer, where a smaller value will give a result closer to the Marquardt-Levenberg **δ**.

At the end of each iteration, $\boldsymbol{\delta}_R$ is calculated, which is a velocity change vector with each component representing an update to the velocity for a single layer. This $\boldsymbol{\delta}_R$ added to

the initial model Vs vector, providing a new starting model for the next inversion iteration. The inversion iterates until the error (equation 11) is minimized.

## PRIDDIS THUMPER EXPERIMENT

### Experiment

The purpose of this field experiment was to test the remote controls for the thumper source, and to acquire multicomponent VSP data, along with near-offset seismic data. It was not designed with near surface characterization in mind. The source used is the CREWES thumper, a multi-component accelerated weight drop source (Lawton et al., 2013). A 100 kg hammer is accelerated by compressed nitrogen, with pressures adjustable from 500 to 2000 psi. The hammer can impact the ground at vertical incidence as a P-wave source, or at ± 45 degrees for generating P and S-waves simultaneously, shown in Figure 1. Data was recorded using all three source orientations, however only the vertical incidence records are used in the research summarized in this chapter.

Data are recorded over a 200 m long seismic line, with 40 10 Hz, 3 component geophones spaced at 5 m (Figure 2). Data are also recorded in a vertical well at the South end of the line, but this is not used in this study. Unfortunately, the shallowest 30 m of sonic well log measurements in this well are inaccurate due to poor cement in this interval. 2 shots are taken at each source location, which are 2 m to the East of the receiver positions. Compared to an ideal MASW survey, this experiment is over a receiver line twice as long (100m typical), with more than double the receiver spacing (2m typical), using 10 Hz geophones rather than lower frequency (4.5 Hz or lower) receivers. The length of the receiver line shouldn't be an issue for applying MASW techniques, and the receiver spacing can be handled using interpolation as described in Mills and Innanen (2016). The geophone frequency will limit the depth of investigation; however, the data will still yield information about the shallow near surface.

FIG. 1. CREWES Thumper source. Shown in S-wave generating mode, at 45° incidence.

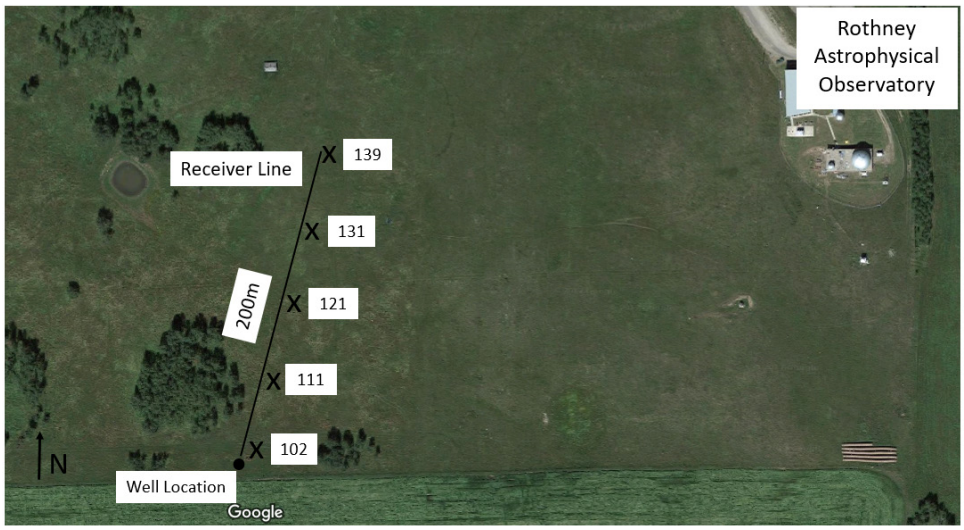


FIG. 2. Field location map. Source locations marked with X and source point number.

## Data and Results

The shot records from the source points at the ends of the receiver lines are shown in Figure 3 (145, South end) and Figure 4 (139, North end). AGC has been applied to these shot records for viewing. The ground roll is the dominant high amplitude signal. In both plots, the average velocity of the Rayleigh waves is ~215 m/s. Slight asymmetry is visible in the records, particularly at near offsets in Figure 3, indicating lateral heterogeneities in the near surface.

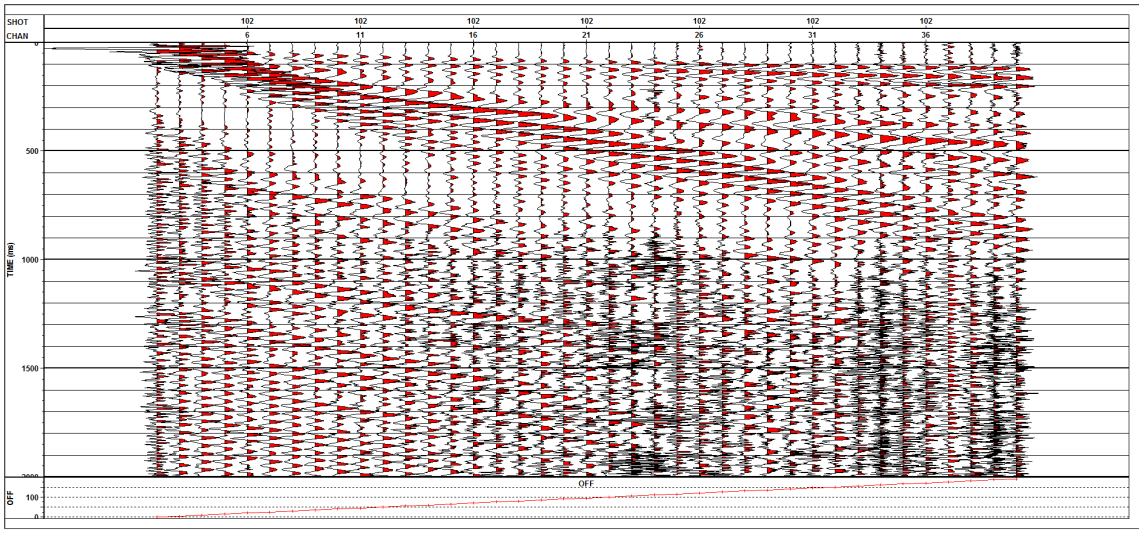


FIG. 3. Shot 145, Source Point 101 at the South end of the line. AGC applied.

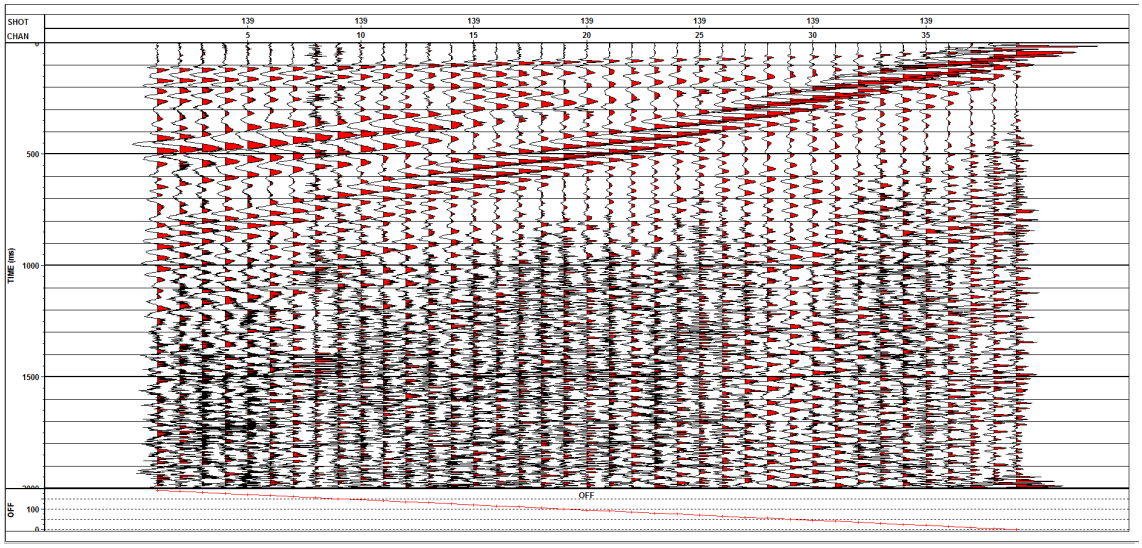


FIG. 4. Shot 139, Source Point 139 at the North end of the line. AGC applied.

Individual shot records are used for the analysis of the Priddis thumper data. Data are evaluated at five source locations, with 2 shots at each. The processing flow is as follows: Shot records generated at the same source point are stacked to reduce noise relative to the ground roll signal. The shot record is then LNMO corrected to flatten the ground roll events before interpolation. Interpolation is preformed twice in this case, resampling the data from 5 m to 1.25 m receiver spacing. The LNMO correction is then reversed, and the data are FK filtered to remove any remaining aliasing.

Once the shot records have been processed, dispersion curves can be generated for the positive and negative offset components of each record. The offset ranges available from each shot record are displayed in Table 1. Offsets to the North of the source are denoted as positive. Despite up to 50 m of offset being available to the North of source point 131, and South of source point 111, it was found that this was insufficient for generating pickable, usable dispersion curves. Park et al. (1999) states that Rayleigh waves can only be treated as horizontally travelling plane waves after they have propagated at least half of their maximum wavelength ($\lambda_{max}$). Below this distance, lower frequencies lack linear coherency. This is observed in the dispersion spectra for the South offsets of source point 111 (Figure 5), where the fundamental mode dispersion curve loses coherence below 20 Hz. For this reason, only data with $\geq$~100 m of offset will be used to generate dispersion curves from which Vs will be inverted for.

Table 1. Offset ranges for each station seismic record.

| Station # | Shot # | Positive (N) Offset (m) | Negative (S) Offset (m) |
|---|---|---|---|
| 139 | 139, 140 | 5 | 195 |
| 131 | 115, 116 | 45 | 155 |
| 121 | 85, 86 | 95 | 105 |
| 111 | 55, 56 | 150 | 50 |
| 102 | 145, 146 | 195 | 5 |

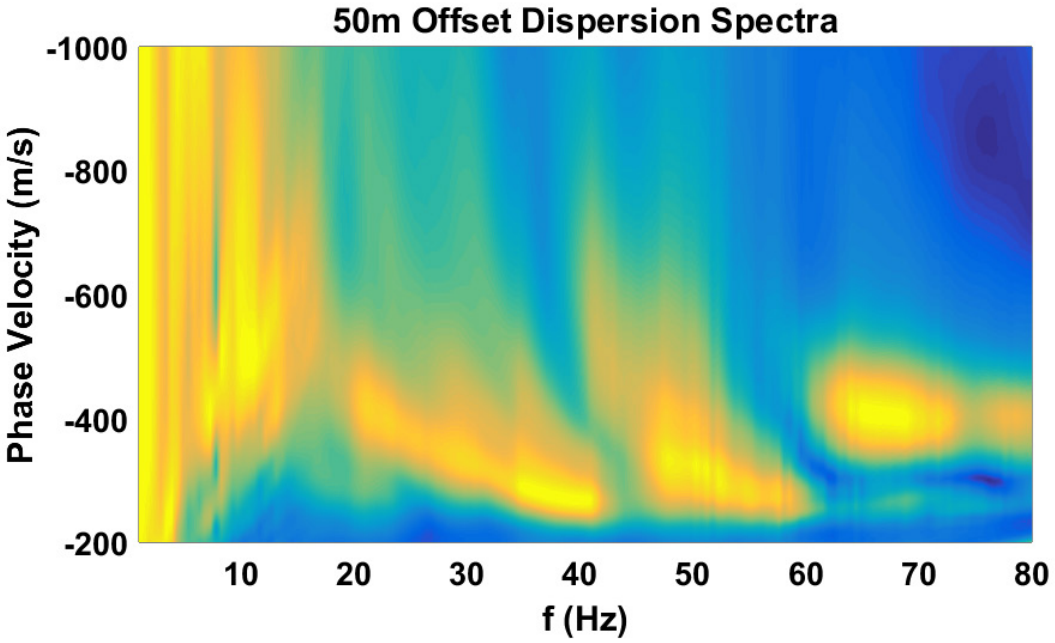


FIG. 5. Dispersion Spectra generated from near offset (<50m) from station 111 (S). Observe the loss of coherency below 25Hz due to the near offset effect.

*Source point 139*

I will proceed with the dispersion analysis starting from the North end of the survey line. The shot record for shot 139 is shown above in Figure 4. The dispersion spectra generated from this raw record is shown in Figure 6. Here the fundamental mode curve can be seen clearly, however, there is a discontinuity in the curve at 40 Hz. Following the process outlined above, the interpolated and filtered record is shown in Figure 7, and from this, a better dispersion curve result can be achieved, shown in Figure 8. The curve is now continuous from 10-60 Hz. Dispersion information is unreliable below 10Hz, due to the bandwidth of the receivers used. Because of this, this inversion is limited to data above 10 Hz. Similar restrictions will be placed on the data at other source points, depending on their quality.

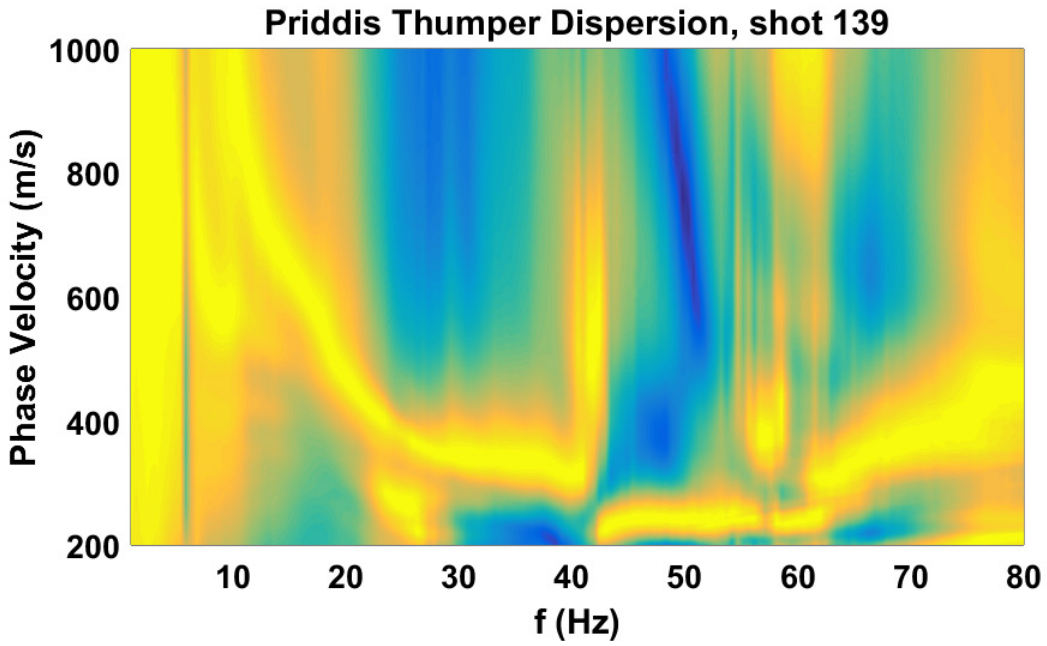


FIG. 6. Dispersion spectra from shot 139. Note discontinuity in dispersion curve at 40Hz.

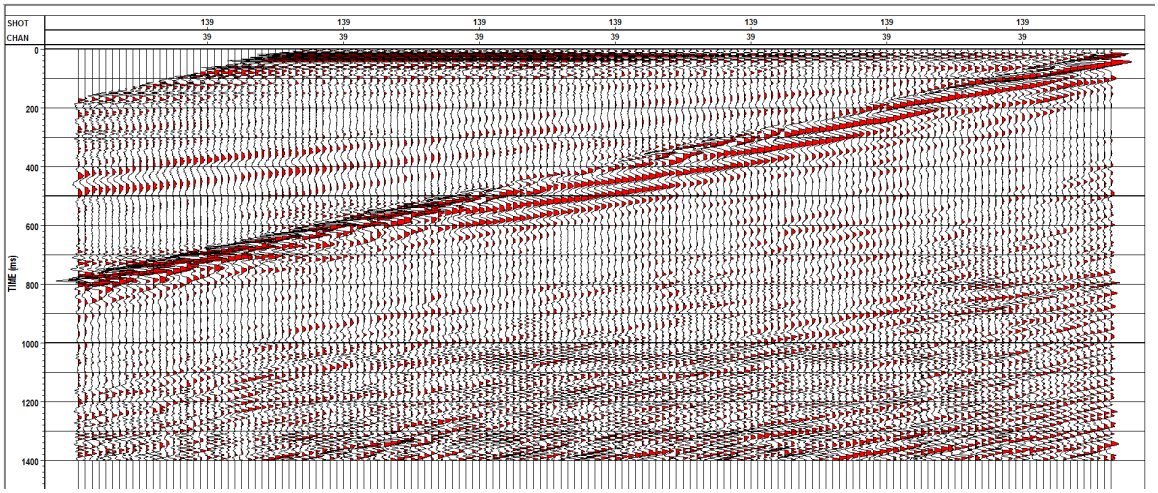


FIG. 7. Source point 139 data interpolated to 1.25m receiver spacing. AGC applied.

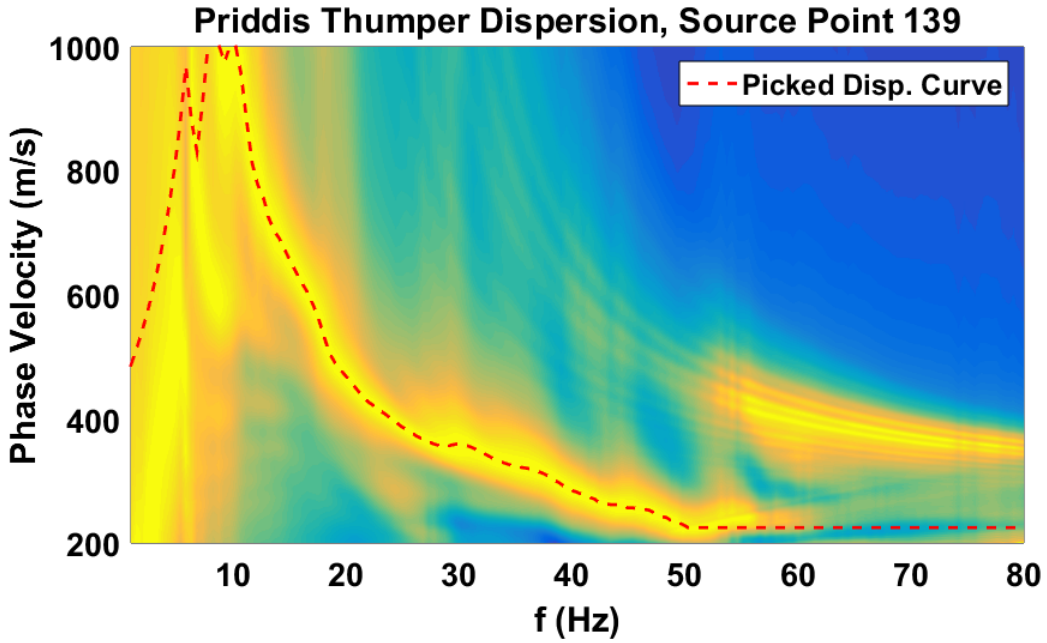


FIG. 8. Dispersion spectra after processing. Picks are erroneous below 10Hz.

Proceeding with the shear wave velocity inversion, a 1D Vs profile can be generated from this dispersion curve, shown in Figure 9. 15 inversion iterations were run, at which point only marginal reductions in the residual were observed (Figure 11). An arbitrary number of layers (9) was chosen for the velocity model, based on the length of the dispersion curve. The half-space, or bedrock appears to be sampled at 22m depth, where the velocity profile flattens, showing only minor velocity variations. There is a roughly linear increase in Vs with depth from surface down to the bedrock. The measured and inverted dispersion curves are shown in Figure 10. Note the separation between 10-20 Hz, which is caused by several factors. First, the measured dispersion curve does not asymptotically approach an upper limit velocity due to the non-measurement of <10 Hz signal. Because of this, the inversion is attempting to match artificially high velocities at low frequencies. Second, the regularization is placing a priority on limiting the change in velocity from layer to layer. Without the regularization, the inversion predicts unreasonably high velocities at these deeper points. Third, the inversion predicts a smooth dispersion curve, so will try to match the curve as closely as possible at all points.

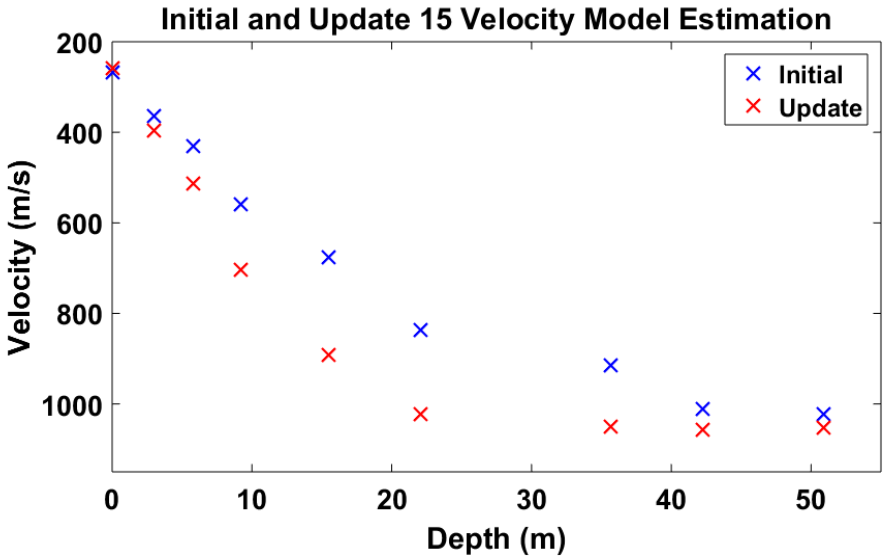


FIG. 9. Shear wave velocity inversion results for source point 139.

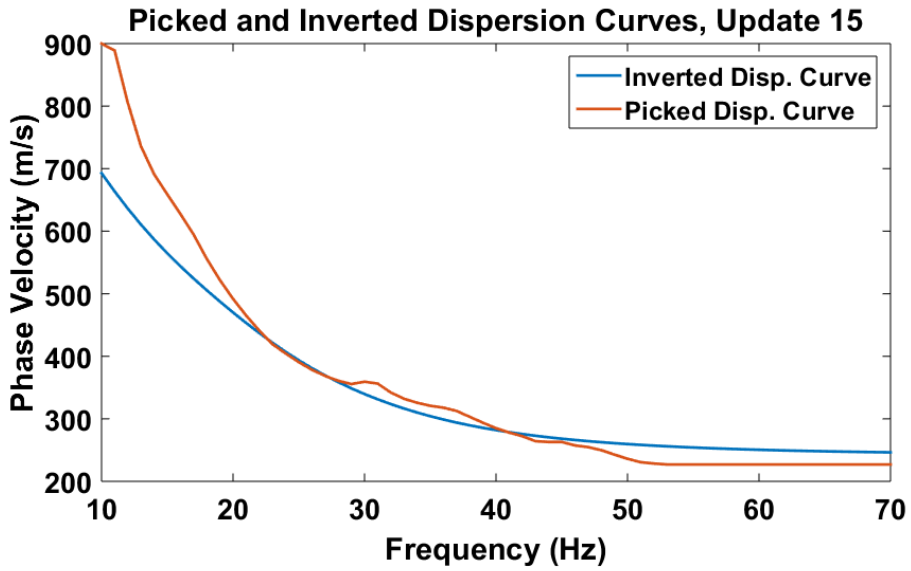


FIG. 10. Dispersion curve inversion results for source point 139.

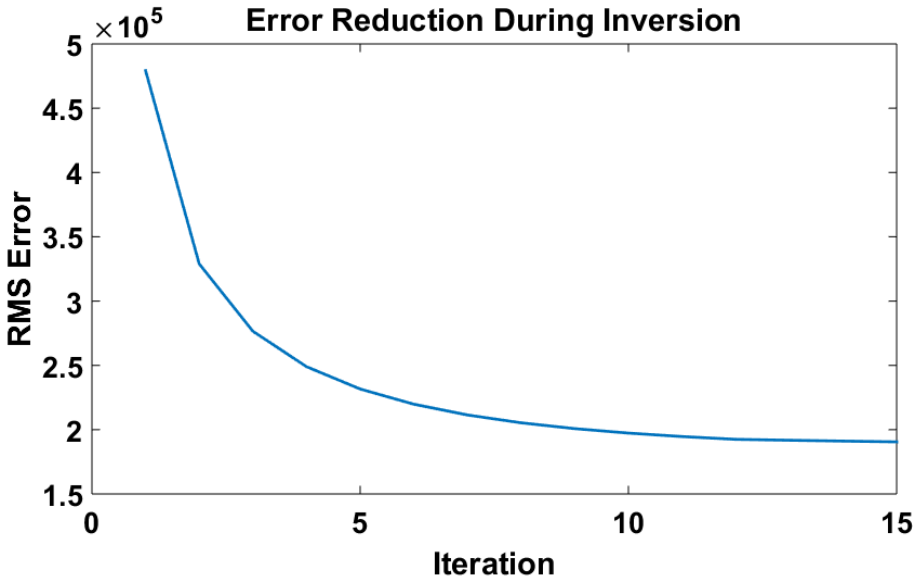


FIG. 11. Residual reduction curve for source point 139.

*Source point 131*

Located approximately 50 m South of source point 139 is Source point 131. The same process applied to the source point 139 data is applied to the data acquired here, and the resulting shot record is shown in Figure 12. Note that only the data to the left of the source point (negative offsets) will be used for this location, due to the limited positive offsets. The dispersion spectra generated from the processed source point 131 records is shown in Figure 12. Similar to source point 139, dispersion trends are not visible below 10 Hz, and any dispersion curve picks below this are erroneous and excluded from the inversion.

Again, 15 inversion iterations were run to produce a 1D Vs profile at this location, shown in Figure 14c. Like source point 139, at 22 m depth the velocity model flattens at ~1020 m/s, suggesting this is the depth and shear wave velocity of the bedrock. Differences between the picked and inverted dispersion curves in Figure 14a arise from the same causes identified for source point 139.

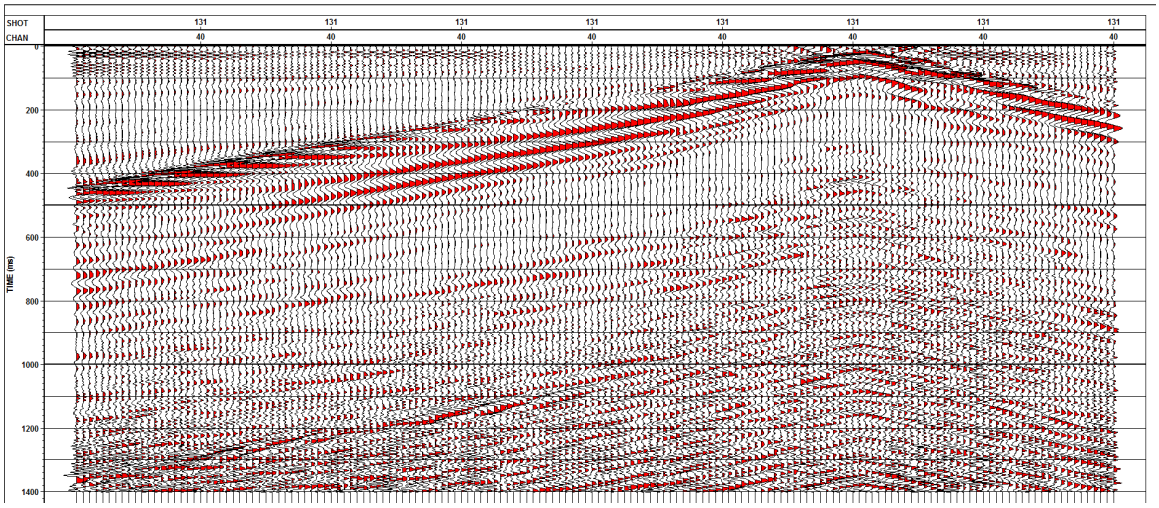


FIG. 12. Source point 131 data interpolated to 1.25m receiver spacing. AGC applied.

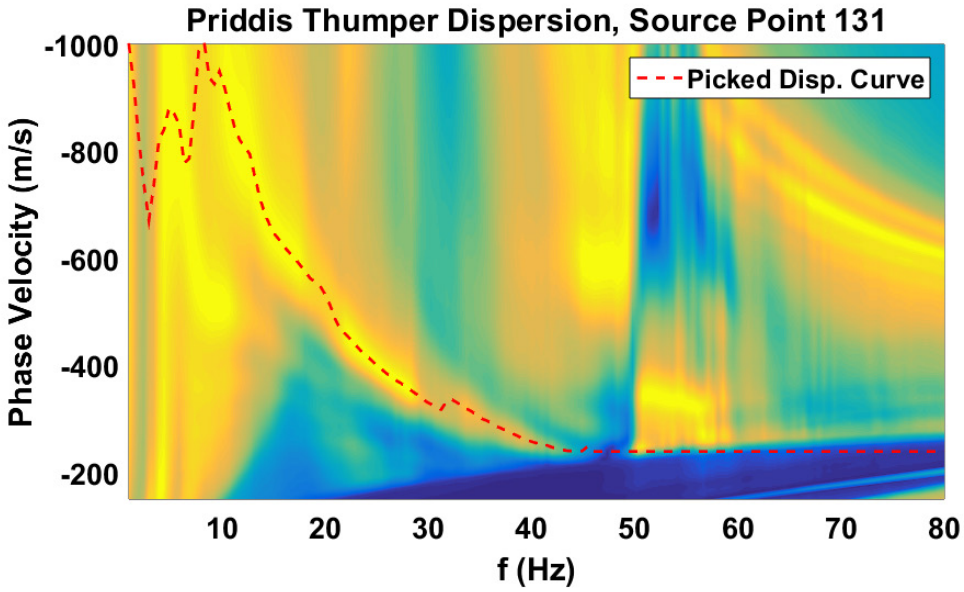


FIG. 13. Dispersion spectra after processing. Picks below 10 Hz are erroneous.

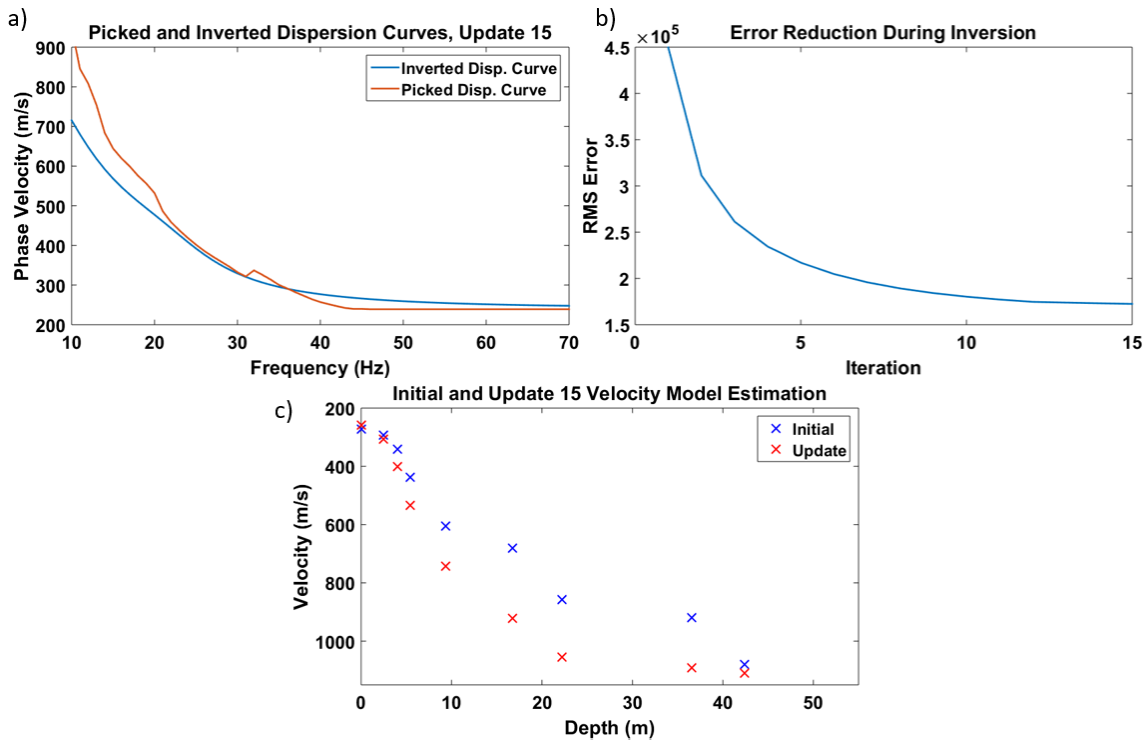


FIG. 14. Inversion results for source point 131. a) Dispersion curve comparison. b) Residual reduction. c) Shear wave velocity model.

*Source point 121*

Source point 121 lies roughly at the centre of the survey line, with ~100 m offset of available data on both sides of the source. This station will contribute two velocity profiles, one from the positive offset data, and one from the negative offset data. The processed and interpolated data are shown in Figure 15. Analysis of this source point is split into positive and negative offset dispersion analysis. As can be seen in Figure 16, the dispersion spectra generated from the positive (b) and negative (a) offsets are quite different. At high (>50 Hz) frequencies in Figure 16a, the dispersion curve is interrupted, so is extrapolated straight out from the its value at 50 Hz, whereas in Figure 16b, the curve continues to decline past 50 Hz. This discrepancy will only affect the velocity prediction for the shallowest layers. For positive offsets, frequencies below 12 Hz are unsampled, versus 10 Hz for the negative offset data. Low frequency phase velocities are also much higher at positive offsets. For example, at 12 Hz, the phase velocity is 944 m/s at positive offset, while at the same frequency it is 687 m/s at negative offsets. As a result, it is likely velocities will be higher to the North of the source point.

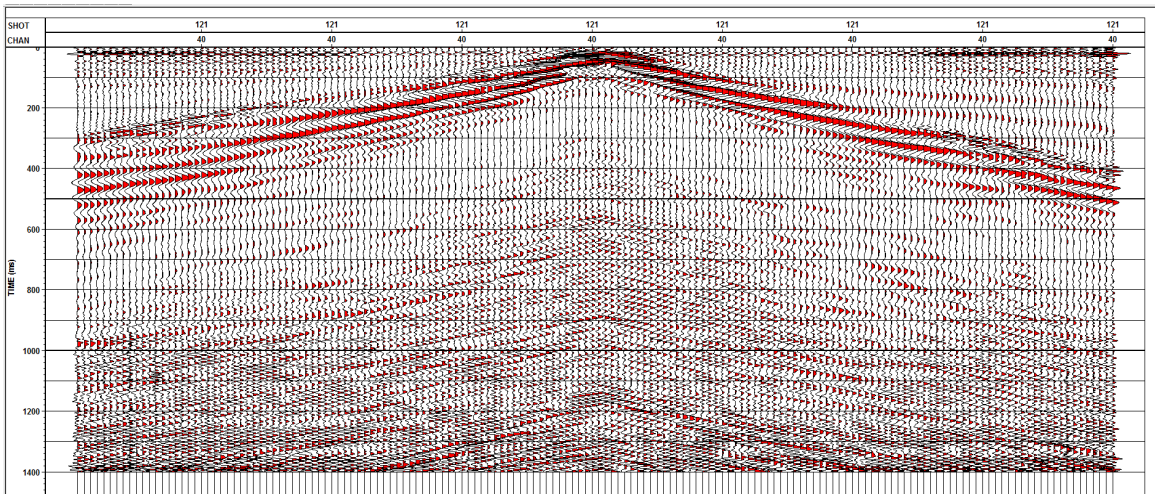


FIG. 15. Source point 121 data interpolated to 1.25m receiver spacing. AGC applied.

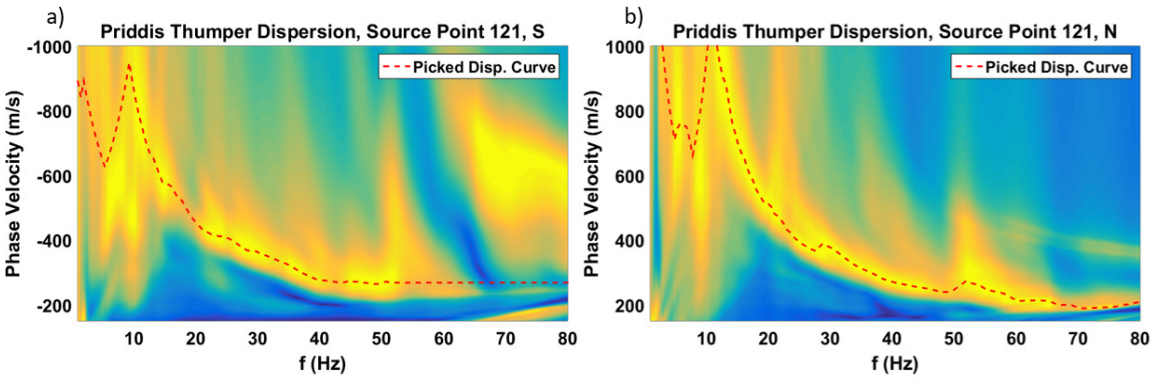


FIG. 16. a) Dispersion spectra for negative offset data. b) Dispersion spectra for positive offset data.

For both the positive and negative offset data, 15 velocity inversion iterations were run. Positive offset data was limited to frequencies >12 Hz, and deeper velocities were unsampled as a result. However, below 20 m depth the velocity profile again flattens (Figure 17c), indicating that deeper strata is bedrock. Again, there is a gradational increase in velocity with depth in the shallower section.

The negative offset data was limited to frequencies >10 Hz, and again shows layers deeper than 20 m depth have approximately equal shear wave velocity (Figure 18b). As predicted from dispersion curves before the inversion, shallower layers have higher velocities to the North of the source point. At 10 m depth, the predicted Vs is ~750m/s to the North, while in the South the predicted velocity is ~100 m/s slower.

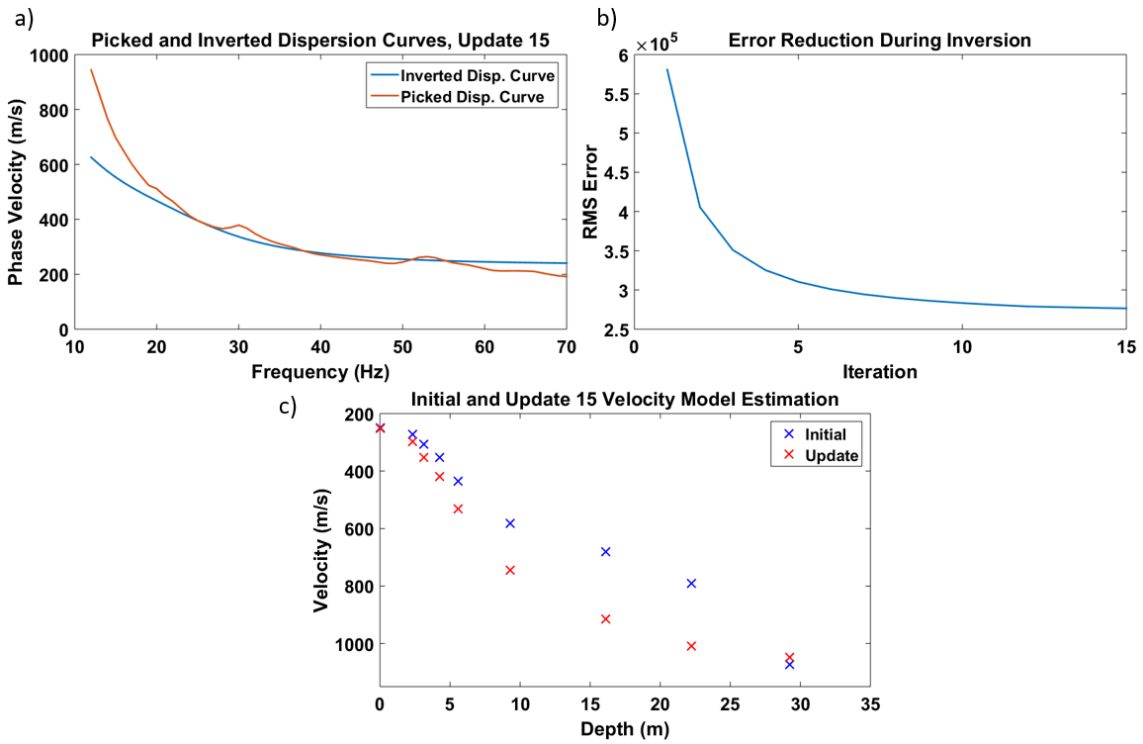


FIG. 17. Inversion results for source point 121, North (positive) offsets. a) Dispersion curve comparison. b) Residual reduction. c) Shear wave velocity model.

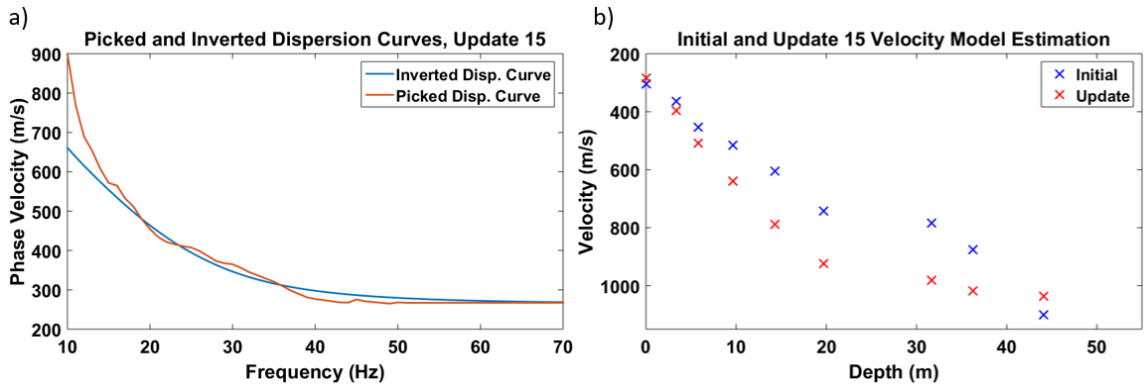


FIG. 18. Inversion results for source point 121, South (negative) offsets. a) Dispersion curve comparison. b) Shear wave velocity model.

*Source point 111*

Source point 111 is 50 m North of the South end of the survey line, and will be used in the North offset velocity profile. The stacked and interpolated shot record is shown in Figure 19. Note that beyond ~100 m offset from the source, ground roll is incohesive. The dispersion spectra generated from this record is shown in Figure 20. The inversion results are shown in Figure 21, where again I observe a relatively linear increase in velocity with depth down to 20 m, where the profile flattens.

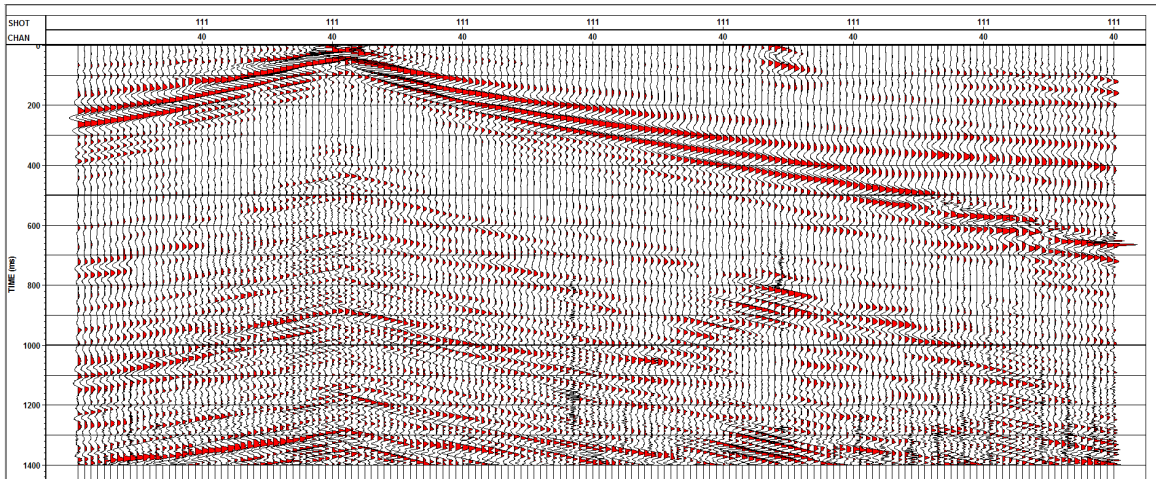


FIG. 19. Source point 111 data interpolated to 1.25m receiver spacing. AGC applied.

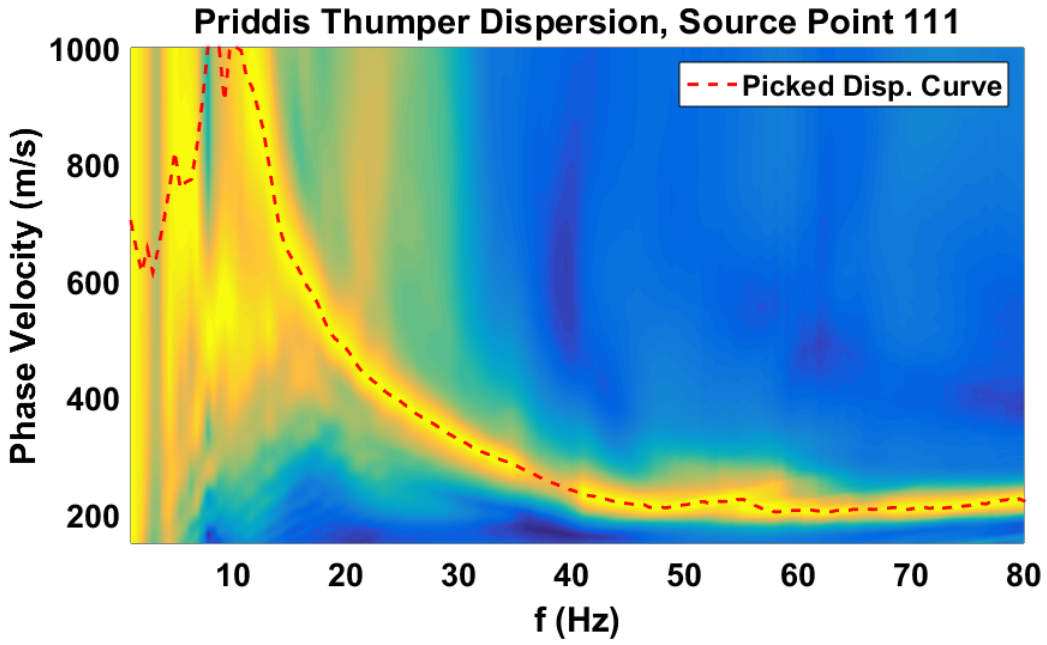


FIG. 20. Dispersion spectra after processing. Picks below 11 Hz are erroneous.

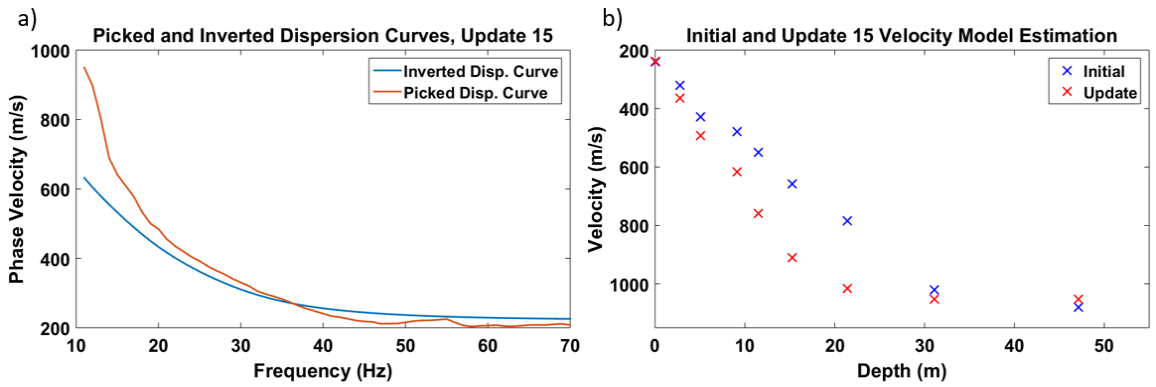


FIG. 21. Inversion results for source point 111. a) Dispersion curve comparison. b) Shear wave velocity model.

*Source point 102*

Source point 102 is the Southern-most point on the survey line, adjacent to the vertical well at the research site. The stacked and interpolated shot record is shown in Figure 22. Again, at offsets greater than ~100 m, dispersion energy is incoherent. The dispersion spectra with picked fundamental mode curve is shown in Figure 23. The inversion results in Figure 24 are very similar to the results at other source points, again indicating a base of near surface or top bedrock at around 20 m depth.

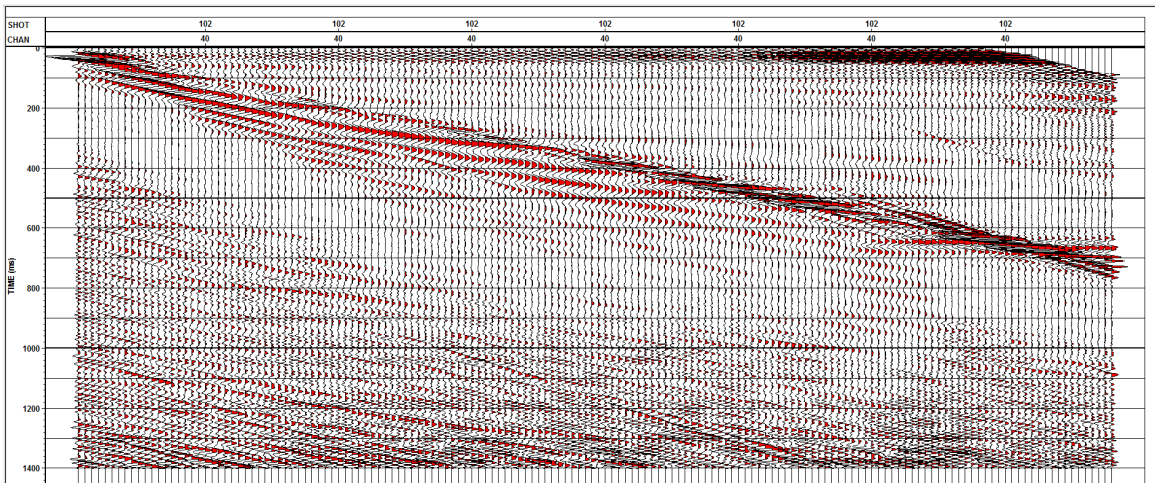


FIG. 22. Source point 102 data interpolated to 1.25m receiver spacing. AGC applied.

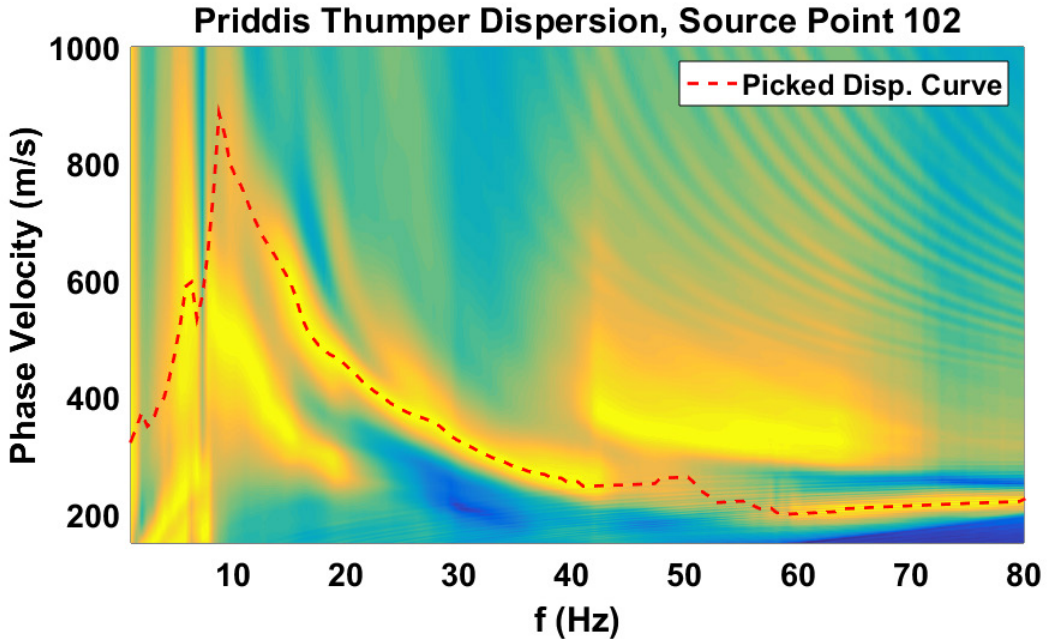


FIG. 23. Dispersion spectra after processing. Picks below 10 Hz are erroneous.

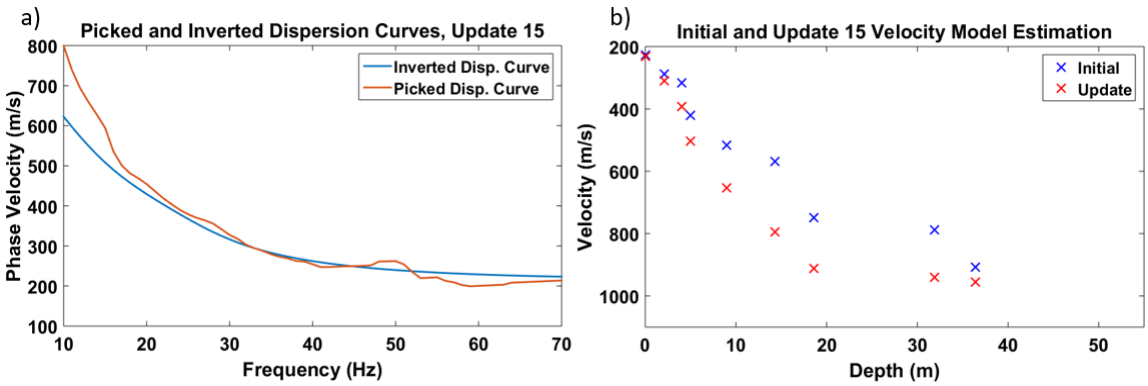


FIG. 24. Inversion results for source point 102. a) Dispersion curve comparison. b) Shear wave velocity model.

*2D velocity profile*

Using the 1D velocity profiles generated at each source point, a 2D shear wave velocity profile can be built over the survey line. Inverted velocity values and depths are used as point velocities, and bilinear interpolation, linear interpolation in both depth and offset, is used to infill velocities between measurements. The 1D profiles are placed 15 m ahead of the source point they were generated from, to be more representative of the geology being sampled by each shot (Figure 25). The 15 m at each end of the survey line is extrapolated from the nearest 1D profile. The 2D shear wave velocity profile is shown in Figure 26, and a zoomed image showing the near surface above the bedrock is in Figure 27.

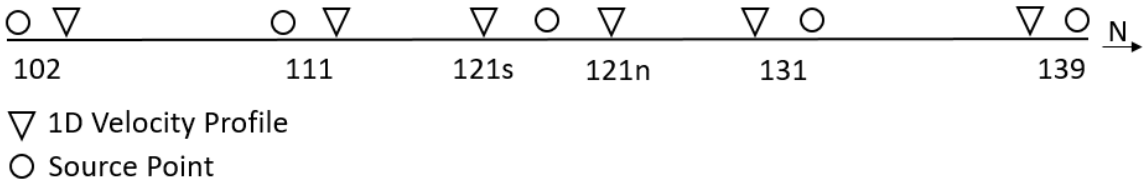


FIG. 25. Survey geometry, with 1D velocity profile location. Source points and their associated 1D profile locations numbered.

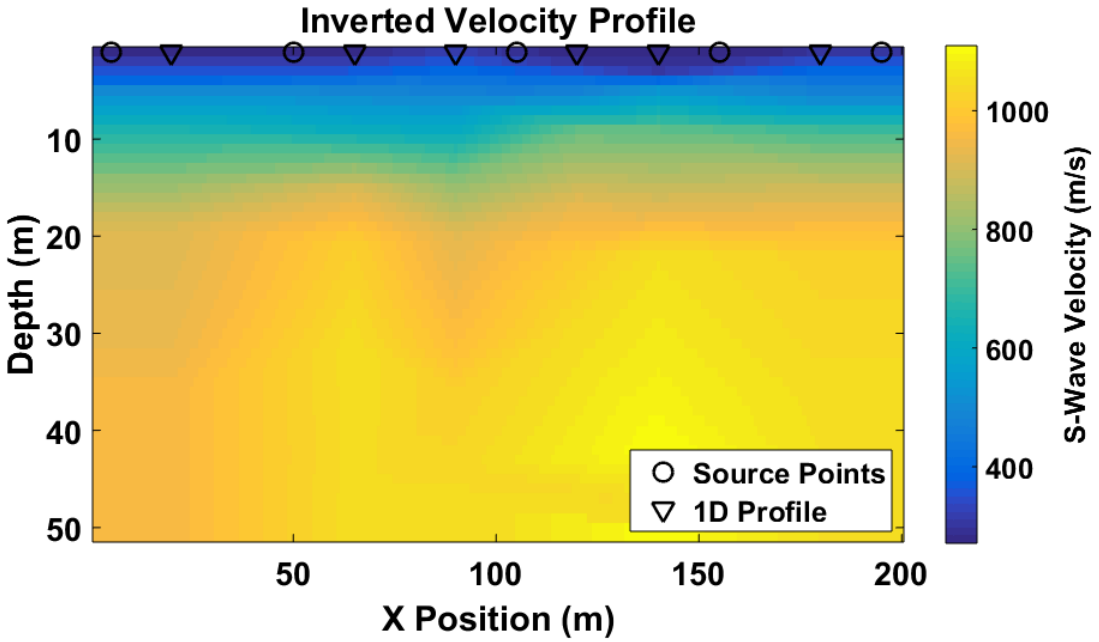


FIG. 26. Inverted shear wave velocity profile, with source and 1D profile locations.

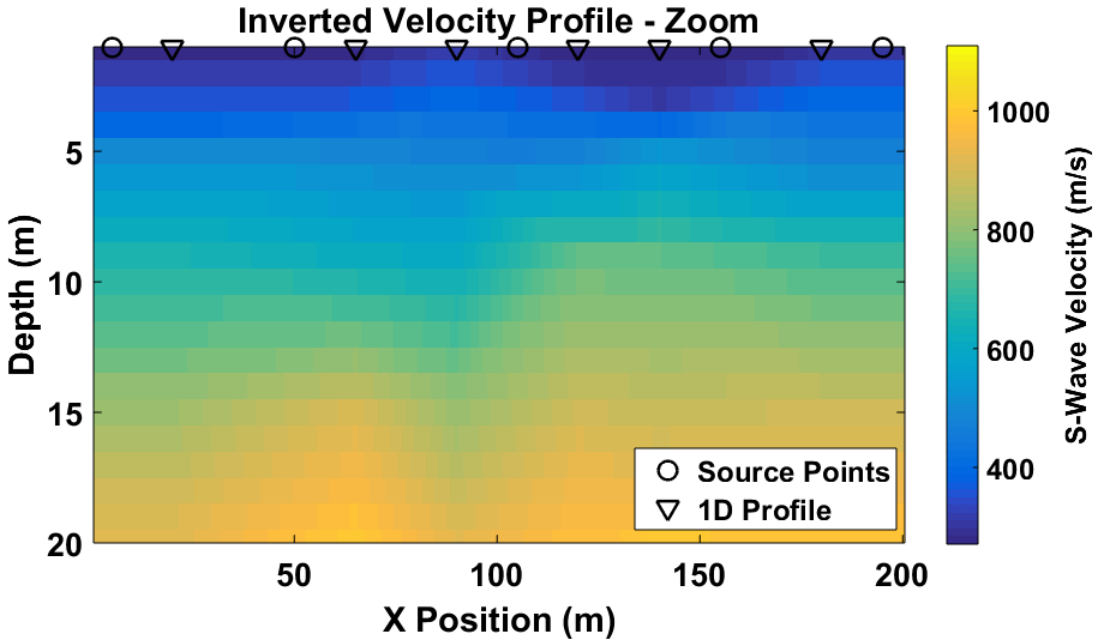


FIG. 27. Unconsolidated near surface zoom of the above profile.

The above velocity profile shows very low shear velocities from 0 to 10 m, an increase in Vs from 10 to 20 m, and high velocities characteristic of bedrock below 20 m depth. This is reasonable for the study area, and is supported by cuttings from a shallow well on the same site (Dulaijan, 2008). The lithology from this well is displayed in Figure 28. At greater than 30 m depth, P-sonic logs from this well have an average velocity of 2600 m/s. With a Vp/Vs of 2.6, which is reasonable for sandstones (Rider and Kennedy, 2011), these velocities are consistent with the inverted Vs of ~1000 m/s at these depths.

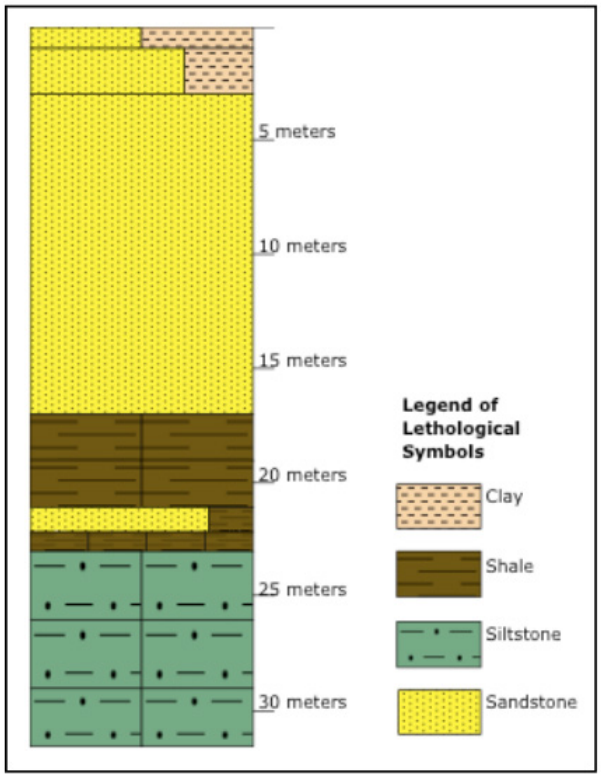


FIG. 28. Lithology log from a shallow Priddis well. From Dulaijan, 2008.

## CONCLUSIONS

In this study, MASW techniques were applied to a field data set acquired with non-ideal acquisition parameters to produce near surface shear wave velocity profiles. Shot records from the same source location were stacked, interpolated to 1.25 m receiver spacing, FK filtered, and inverted for 1D Vs profiles. These profiles were then interpolated in both depth and the offset direction to produce a 2D velocity profile over the survey line. This validates the effectiveness of the developed processing method on field data, and on data with non-ideal sampling. The estimated near-surface velocity profile's depth to bedrock is consistent with drill cuttings from a near-surface borehole on the site.

## ACKNOWLEDGEMENTS

The authors thank the sponsors of CREWES for continued support. This work was funded by CREWES industrial sponsors and NSERC (Natural Science and Engineering Research Council of Canada) through the grant CRDPJ 461179-13.

## REFERENCES

Dulaijan, K.A., 2008, Near-surface characterization using seismic refraction and surface-wave methods, MSc thesis, University of Calgary.

Lawton, D.C., Gallant, E.V., Bertram, M.B., Hall, K.W., and Bertram, K.L., 2013, A new S-wave seismic source, CREWES Research Reports, Volume 25.

Lines, L.R., and Treitel, S., 1984, Tutorial: A review of least-squares inversion and its application to geophysical problems, Geophysical Prospecting, **32**, 159-186.

Mills, A., Cova, R., and Innanen, K., 2016, Surface wave modelling and near surface characterization background, CREWES Research Reports, Volume 28.

Mills, A., and Innanen, K., 2016, Processing of ground roll for the study of near-surface Rayleigh wave dispersion, CREWES Research Reports, Volume 28.

Park, C.B, Miller, R.D., and Xia, J., 1999, Multichannel analysis of surface waves, Geophysics, **64**, No. 3, 800-808.

Rider, M., and Kennedy, M., 2011, The geological interpretation of well logs, Rier-French Consulting.

Stokoe II, K.H., Wright, G.W., Bay, J.A., and Roesset, J.M., 1994, Characterization of geotechnical sites by SASW method, *in* Woods, R.D., Ed., Geophysical characterization of sites: Oxford Publishers.

Virieux, J., and Operto, S., 2009, An overview of full-waveform inversion in exploration geophysics, Geophysics, **74**, No. 6, WCC1-WCC26.

Xia, J., Miller, R.D., and Park, C.B., 1999, Estimation of near-surface shear-wave velocity by inversion of Rayleigh waves, Geophysics, **64**, 691-700.